Post-plasma Quenching to Improve Conversion and Energy Efficiency in a CO_2 Microwave Plasma

E.R. Mercer*[1] and S. Van Alphen*[1,4], C.F.A.M. van Deursen[2], T.W.H. Righart[3], W. Bongers[2], R. Snyders[4,5], A. Bogaerts[1], M.C.M. van de Sanden[2], and F.J.J. Peeters[2].

[1]Research group PLASMANT, Department of Chemistry, University of Antwerp, Universiteitsplein 1, 2610 Antwerpen, Belgium

[2]Research Group PSFD, Dutch Institute of Fundamental Energy Research, De Zaale 20, 5612 AJ Eindhoven, Netherlands

[3]Maastricht University, P.O. Box 616, 6200 MD Maastricht, Netherlands

[4]Research group ChIPS, Department of Chemistry, University of Mons, 20, Place du parc, 7000 Mons, Belgium

[5]Materia Nova Research Center, 3 Avenue Nicolas Copernic, 7000 Mons, Belgium

Email: elizabeth.mercer@uantwerpen.be; senne.vanalphen@uantwerpen.be; F.J.J.Peeters@differ.nl

Section S.1 Chemistry

The evolution of the species densities as a function of time is described by:

$$\frac{\partial c_i}{\partial t} = \sum_j a_{ij} r_j \qquad \text{[S.E1]}$$

in which c_i is the concentration of species *i* (mol.m^{-3}), and *j* is the number of reactions included in the model. The stoichiometric coefficients are denoted as a_{ij}, and are defined as being negative for reactants and positive for products. The reaction rates (r_j, mol/(m^3·s) $^{-1}$) can be described by the mass action law:

$$r_j = k_j^f \prod_\mathrm{i} \mathrm{c}_\mathrm{i}^{-\mathrm{a}_{ij}} - k_j^r \prod_\mathrm{i} \mathrm{c}_\mathrm{i}^{\mathrm{a}_{ij}} \qquad \text{[S.E2]}$$

Here, k_j^f and k_j^r represent the forward and reverse rate coefficients, respectively. The reactions included in the model are shown in *Table S.T1*. This set only includes thermal reactions of species that play a significant role in the thermal dissociation and recombination pathway of CO_2. The rate coefficients of the forward rates, shown in *Table 1*, are taken from the Gri-mech 3.0 database [1], while the rate coefficients of the reverse rates are calculated assuming thermodynamic equilibrium:

$$k^r = \frac{k^f}{K_{eq}} \qquad \text{[S.E3]}$$

In which K_{eq} is the equilibrium constant of the reaction calculated using thermodynamic constants of the NASA-Glenn database [2].

Table S.T1 | List of reactions and reaction rate coefficients of the forward reactions used in the model, as adopted from the Gri-mech 3.0 database [1]. *The rate coefficients of the backward reactions are calculated assuming thermodynamic equilibrium. Presented below, R is defined as 1.9872 cal(K.mol)$^{-1}$, c_M is given in mol.cm^{-3}, and T in K.*

Reaction	*Reaction rate coefficient of forward reaction*
$CO + O + M \rightarrow CO_2 + M$	$k = \dfrac{k_{inf}}{1 + \dfrac{k_{inf}}{k_o c_M}}$

	$k_{inf} = 1.80 \text{ x } 10^{10}\ [\mathrm{cm^3 mol^{-1}} s^{-1}] \exp\left(\frac{-2385\ [\frac{cal}{mol}]}{RT}\right)$ $k_o = 6.02 \text{ x } 10^{14}\ [\mathrm{cm^6 mol^{-2}} s^{-1}] \exp\left(\frac{-3000\ [\frac{cal}{mol}]}{RT}\right)$
$CO + O_2 \rightarrow CO_2 + O$	$k = 2.50 \text{ x } 10^{12}\ [\mathrm{cm^3 mol^{-1}} s^{-1}] \exp\left(\frac{-47800\ [\frac{cal}{mol}]}{RT}\right)$
$O + O + M \rightarrow O_2 + M$	$k = \frac{1.20 \text{ x } 10^{17}\ [\mathrm{cm^6 mol^{-2}} s^{-1}]}{T}\ c_M$
$C + O + M \rightarrow CO + M$	$k = 7.76 \text{ x } 10^{6}\ [\mathrm{cm^6 mol^{-2}} s^{-1}] \left(\frac{T}{300\ [K]}\right)^{-3.08} \exp\left(\frac{-2114\ [K]}{T}\right) c_M$

Section S.2 Experimental Apparatus

S.2.1 2.45 GHz Microwave Reactor

This work utilizes a 2.45 GHz MW source with a maximum power of 1400 W. The configuration exploits a forward or reverse vortex to confine and stabilize the plasma. The design is based on early work outlined by *V.A. Legasov et al.*, which showed promising results for energy efficiency in the dissociation of CO_2 (*Figure S1*) [3].

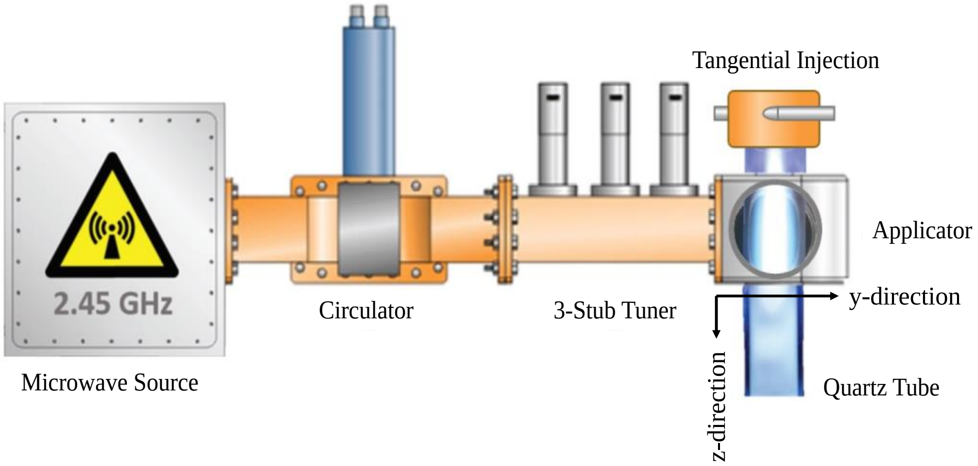

Figure S1 | Overview of 2.45 GHz MW reactor at DIFFER with key components labeled.

The MW reactor utilizes a vortex-stabilized MW reactor with a 2.45 GHz magnetron MW source (Frick und Mallah MKO 2kW AC002). The magnetron emits an adjustable continuous wave (CW) power up to 1400 W at a set frequency transmitted through a WR340 rectangular waveguide in a transverse electric mode (TE_{10}) standing wave, such that the electric field is always at a right angle to the y-direction of the waveguide (*Figure S1*). The CW is applied to a CO_2 gas flow passing perpendicularly through a fused quartz tube, which intersects the waveguide in the z-direction.

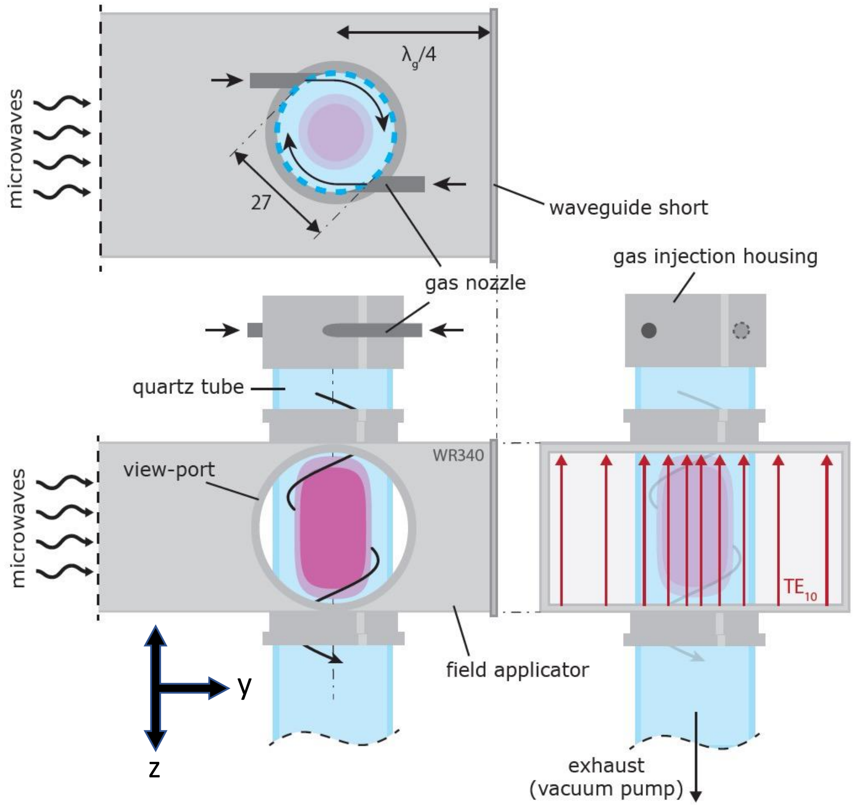

Figure S2 | WR340 waveguide with intersecting quartz tube. The illustration details the tangential gas input and flow geometry (top), field applicator (bottom left), and standing wave (bottom right).

The field applicator is a crucial design aspect of the MW plasma reactor configuration, significantly influencing field localization and strength (*Figure S2*). To produce the TE_{10} standing wave, a sliding waveguide short reflects the transmitted forward wave, granting low radiation losses and high field coupling to the plasma. An automatic stub tuner (HOMER S-TEAM STHT2450) between the magnetron source and quartz tube ensures a high coupling efficiency by matching the impedance of the source to the plasma, such that reflected power remains below 1% during experiments. The absorbed power is computed using an integration of the automatic impedance and power measurement system using the magnitude and phase of the reflection coefficient, incident, reflected/absorbed power, and frequency.

S.2.2 Nozzle Design and Housing

The converging-diverging nozzle, CDN (*Figure S3*), was housed within a special metal casing (*Figure S4*), which was water-cooled.

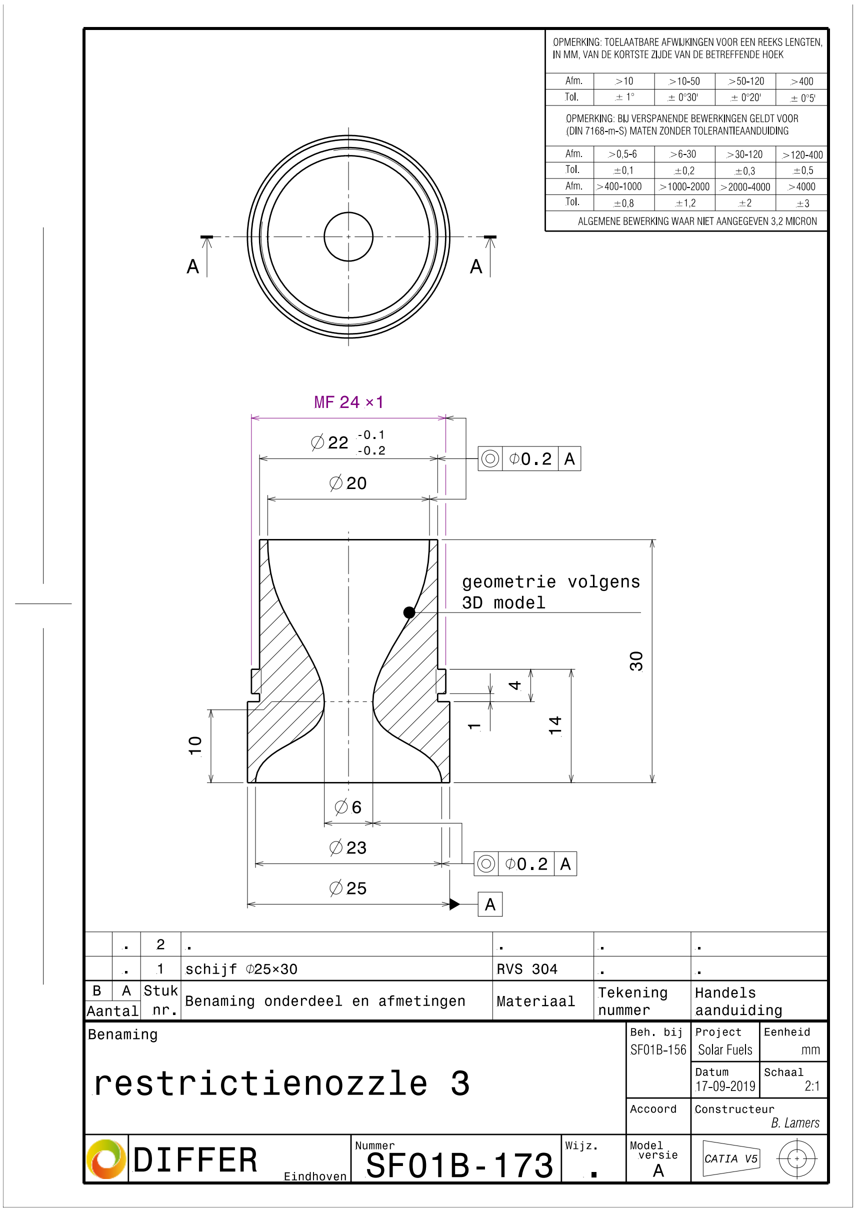

OPMERKING: TOELAATBARE AFWIJKINGEN VOOR EEN REEKS LENGTEN, IN MM, VAN DE KORTSTE ZIJDE VAN DE BETREFFENDE HOEK

Afm.	>10	>10-50	>50-120	>400
Tol.	± 1°	± 0°30'	± 0°20'	± 0°5'

OPMERKING: BIJ VERSPANENDE BEWERKINGEN GELDT VOOR (DIN 7168-m-S) MATEN ZONDER TOLERANTIEAANDUIDING

Afm.	>0,5-6	>6-30	>30-120	>120-400
Tol.	±0,1	±0,2	±0,3	±0,5
Afm.	>400-1000	>1000-2000	>2000-4000	>4000
Tol.	±0,8	±1,2	±2	±3

ALGEMENE BEWERKING WAAR NIET AANGEGEVEN 3,2 MICRON

	.	2	.	.	.	.
	.	1	schijf ϕ25×30	RVS 304	.	.
B	A	Stuk nr.	Benaming onderdeel en afmetingen	Materiaal	Tekening nummer	Handels aanduiding
Aantal						

Benaming restrictienozzle 3	Beh. bij SF01B-156	Project Solar Fuels	Eenheid mm
		Datum 17-09-2019	Schaal 2:1
	Accoord	Constructeur B. Lamers	
DIFFER Eindhoven	Nummer SF01B-173	Wijz. .	Model versie A

CATIA V5

Figure S3 | Schematic drawing of the converging-diverging nozzle.

Only part of the diverging side of the CDN was in contact with the water-cooled wall from the housing (*Figure S4*).

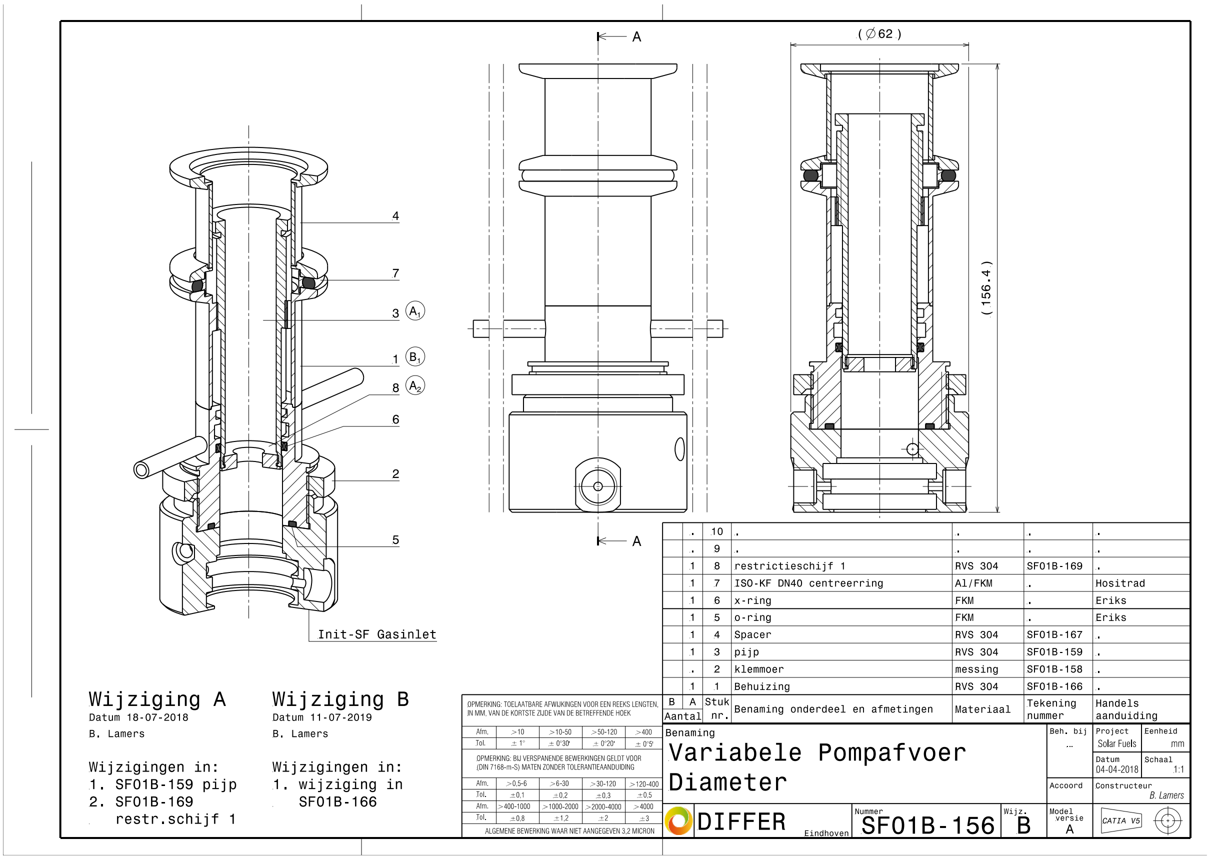

Wijziging A
Datum 18-07-2018
B. Lamers

Wijzigingen in:
1. SF01B-159 pijp
2. SF01B-169
   restr.schijf 1

Wijziging B
Datum 11-07-2019
B. Lamers

Wijzigingen in:
1. wijziging in
   SF01B-166

Aantal B	Aantal A	Stuk nr.	Benaming onderdeel en afmetingen	Materiaal	Tekening nummer	Handels aanduiding
	.	10	.	.	.	.
	.	9	.	.	.	.
	1	8	restrictieschijf 1	RVS 304	SF01B-169	.
	1	7	ISO-KF DN40 centreerring	Al/FKM	.	Hositrad
	1	6	x-ring	FKM	.	Eriks
	1	5	o-ring	FKM	.	Eriks
	1	4	Spacer	RVS 304	SF01B-167	.
	1	3	pijp	RVS 304	SF01B-159	.
	.	2	klemmoer	messing	SF01B-158	.
	1	1	Behuizing	RVS 304	SF01B-166	.

OPMERKING: TOELAATBARE AFWIJKINGEN VOOR EEN REEKS LENGTEN, IN MM, VAN DE KORTSTE ZIJDE VAN DE BETREFFENDE HOEK

Afm.	>10	>10-50	>50-120	>400
Tol.	± 1°	± 0°30'	± 0°20'	± 0°5'

OPMERKING: BIJ VERSPANENDE BEWERKINGEN GELDT VOOR (DIN 7168-m-S) MATEN ZONDER TOLERANTIEAANDUIDING

Afm.	>0,5-6	>6-30	>30-120	>120-400
Tol.	±0,1	±0,2	±0,3	±0,5
Afm.	>400-1000	>1000-2000	>2000-4000	>4000
Tol.	±0,8	±1,2	±2	±3

ALGEMENE BEWERKING WAAR NIET AANGEGEVEN 3,2 MICRON

Benaming
Variabele Pompafvoer Diameter
Beh. bij ...
Project Solar Fuels
Eenheid mm
Datum 04-04-2018
Schaal 1:1
Accoord
Constructeur B. Lamers
DIFFER Eindhoven
Nummer SF01B-156
Wijz. B
Model versie A
CATIA V5

Figure S4 | Schematic of water-cooled nozzle housing.

Due to the limited contact of the CDN with the metal casing, and the unremarkable difference in the measured power lost to water-cooling when the two configurations were compared (without and with the CDN), the cooling of the nozzle is expected to be negligible.

Section S.3 Temperature Measurements

S.3.1 Doppler Broadening Spectroscopy

The core plasma temperature (T_{core}) was determined using the principle of Doppler broadening at 777 nm oxygen triplet emission lines, O($3s^5S^0 \leftarrow 3p^5P$), at 777.539, 777.417, and 777.194 nm. A high-resolution VIPA spectrometer by LightMachinery was utilized alongside a 50.8 mm collection bi-convex lens with a focal distance (f_{pf}) = 100 mm with a broadband anti-reflection coating with a wavelength range between 650 – 1050 nm. The lens was coupled with a 610 nm longpass colored glass filter. A 400 μm multimode optical fiber was used to project the plasma emission onto the entrance slit of the CCD camera. The dispersed emission fed into the CCD camera had a resolution of 0.5 pm(pixel)$^{-1}$, which was used to resolve and analyze the spectral lines.

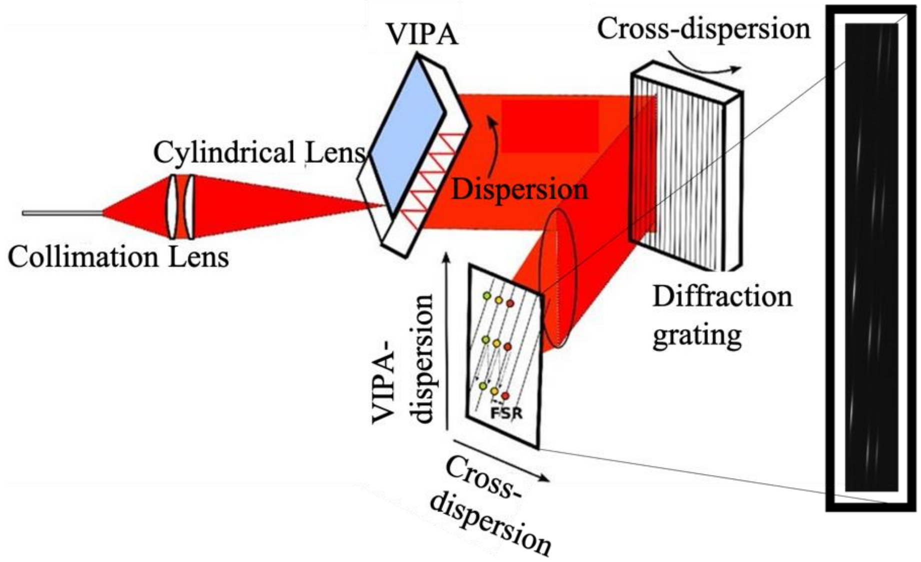

Figure S5 | Etalon VIPA slitting incident beam before diffraction grating gives a raw image.

The light enters the spectrometer through an optical fiber and is dispersed by a VIPA Etalon on the vertical axis with a sub-picometer resolution, followed by a conventional diffraction grating to spread overlapping orders in the horizontal direction. This produces a 2D spectrum of light. LightMachinery software unwraps the spectrum, creating an ultra-high resolution wavelength spectrum (*Figure S5*).

Doppler broadening results from the isotropic thermal motion of particles, leading to a Gaussian spectral broadening component with a standard deviation value on the order of a picometer. This deviation depends on the frequency of the spectral line, the mass of the emitting particle, and the temperature. Using a calibration lamp to measure and void the instrumental broadening, a convolved fitting algorithm was employed to determine the Gaussian and Lorentzian components resulting from the plasma spectrum. The full scope of this fitting procedure, including relevant equations, is outlined in the thesis of *T.W.H. Righart* [4].

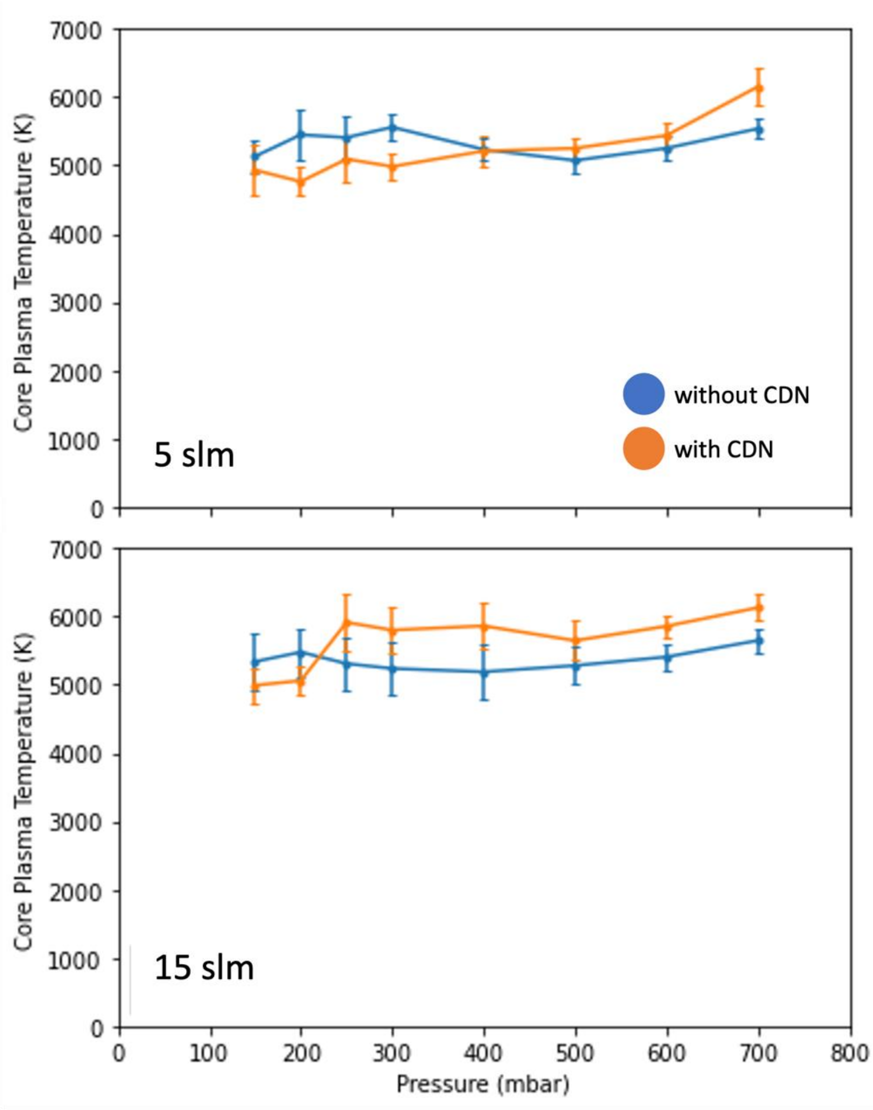

Figure S6 |Comparison of T_{core} as a function of pressure without the CDN (blue) and with the CDN inserted (orange). A higher trend for the T_{core} as a function of pressure is observed with the addition of the CDN. The data for the T_{core} was collected from Doppler broadening spectroscopy.

In *Figure S6*, the addition of the CDN is not seen to affect the T_{core} to a great extent [5]. Flame band spectroscopy was utilized as a secondary spectroscopic measurement to give the radial temperature profile at both the height of the plasma and in the afterglow region before the CDN.

S.3.2 Flame Band Spectroscopy

Doppler broadening is not suitable for measuring temperatures below 2000 K due to the lack of atomic oxygen below that temperature and the lack of energetic electrons to excite atomic oxygen electronically. To accurately measure the temperature around the plasma and the temperature in the afterglow, flame band spectroscopy was utilized as a secondary spectroscopic temperature measurement.

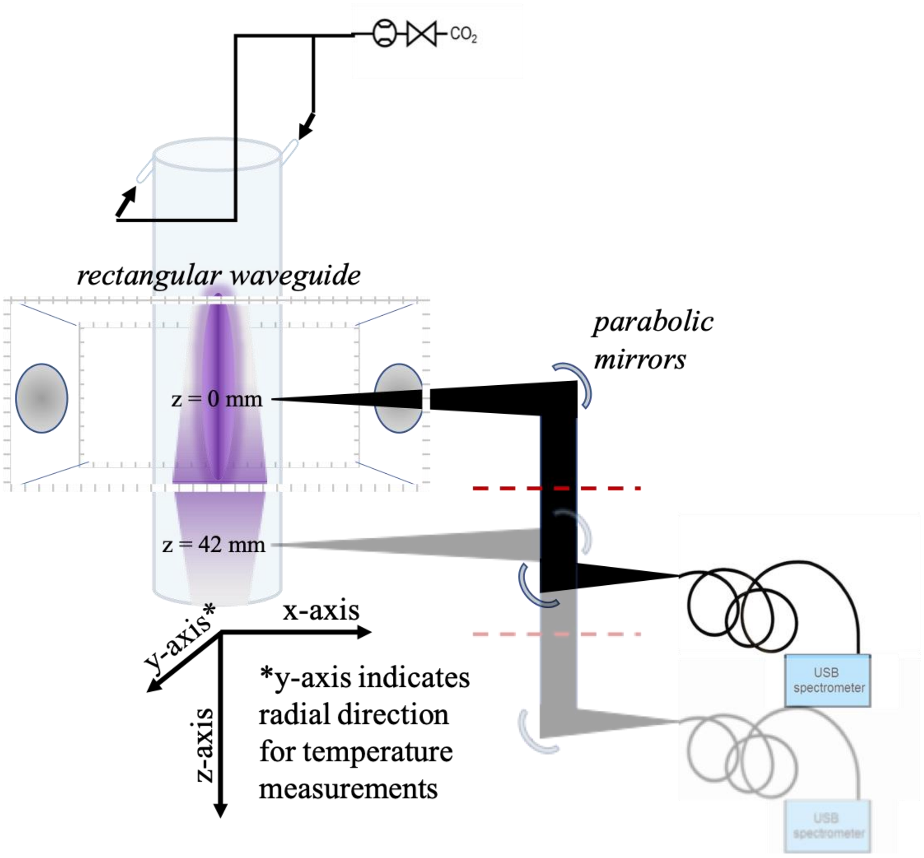

Figure S7 | Schematic drawing of the flame band optical setup, where data was collected in the radial direction along the y-axis at two positions relative to the plasma along the z-axis. The first collection occurred at the height of the plasma, z = 0 mm, and the second, z = 42 mm, downstream of the plasma.

The afterglow was measured along a cylindrical region (*d* = 27 mm) through the quartz tube using an Ocean Optics Flame-S Miniature Spectrometer coupled with two 90° off-axis parabolic UV-enhanced aluminum mirrors with a reflective focal length (RFL) = 50.8 mm (*Figure S7*). The mirrors reflect more than 90% of the 250 – 450 nm light waves. Between the mirrors, an iris with an opening of 6.9 mm sets the solid angle (W) = 1.45 x 10^{-2} sr for collection onto a multimode UV optical fiber (20 cm, 200 mm), which is fed into a 200 mm entrance slit of the spectrometer. The light then moves through a grating blazed at 300 nm. Detailed methods for calibration and discrete inverse Abel transforms are described in *Raposo et al.* [6].

The wavelength-integrated emission intensity (I_γ) from the flame band spectra can be used to obtain the product of the $[O]$ and $[CO]$ concentration through:

$$I_\gamma = k_\gamma(T)[CO][O], \tag{S.E4}$$

where $[CO][O]$ are carbon monoxide and atomic oxygen number densities (m^{-3}) and $k_\gamma(T)$ is assumed equal to $1.14 \times 10^{-24} e^{-\frac{2080}{T}}$ (photons.$\mathrm{m}^{-3}\mathrm{s}^{-1}$). [6]–[8] With temperature (T) known from the wavelength-dependent flame band spectra fitting, [S.E4] can be solved for $[CO][O]$.

To more easily compare different operating conditions, a geometric average of the O and CO fractions (f_O and f_{CO}) is defined by:

$$(f_O f_{CO})^{\frac{1}{2}} = \frac{([CO][O])^{\frac{1}{2}}}{[M]}, \tag{S.E5}$$

with $[M]$ representing the neutral density and is given by:

$$[M] = \frac{p}{k_b T} \tag{S.E6}$$

where p represents the pressure (Pa), k_b represents the Boltzmann constant, and T is the temperature (K).

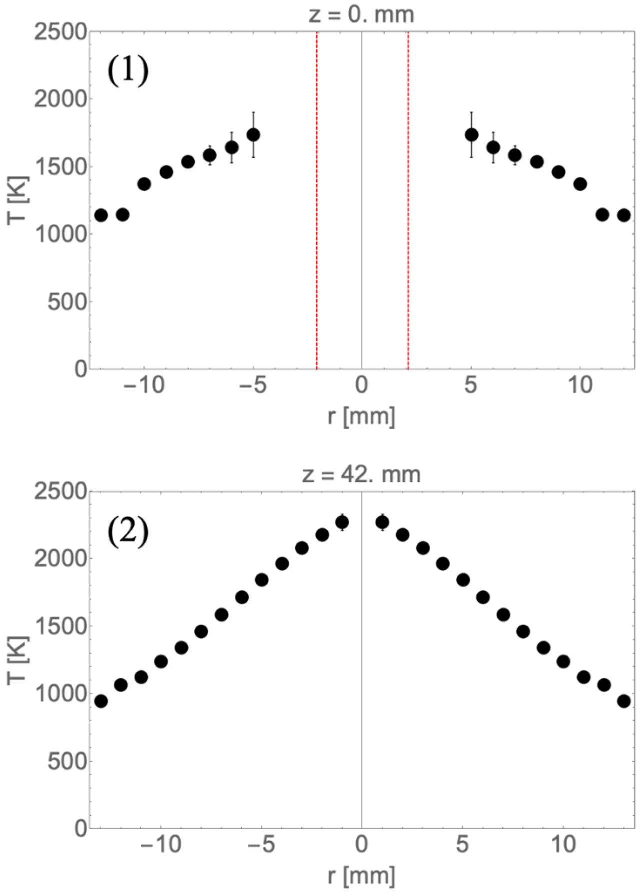

Figure S8 | Flame band spectroscopy temperature data without CDN, 5 slm, 150 mbar, at the height of the plasma (z = 0 mm, (1)) and in the afterglow region (z = 42 mm, (1)). The red lines in (1) indicate the FWHM of the plasma.

In *Figure S8*, the radial temperature profile is given for a flow rate of 5 slm and a pressure of 150 mbar without CDN at the height of the plasma (*Figure S8(1)*) and in the afterglow region

(*Figure S8(2)*). The temperature gradient at the height of the plasma is relatively gradual from the sides to the center, where the data points are no longer visible (*Figure S8(1)*). The red lines in *Figure S8(1)* represent the FWHM of the plasma, indicating a sudden and dramatic increase in temperature due to the plasma since all data points above 2500 K are no longer plotted due to uncertainty in accuracy using flame band spectroscopy. *Figure S8(2)* shows the radial temperature profile in the afterglow region of the plasma at z = 42 mm, where a temperature gradient is still observed. At temperatures above 2000 K, dissociation of CO_2 is still active [9].

Using flame band emission intensity, we can take the geometric average of the O and CO fractions, $(f_O f_{CO})^{1/2}$, above the nozzle at the point of decay seen between 300 and 400 mbar at ϕ = 5 slm (*Figure S9*).

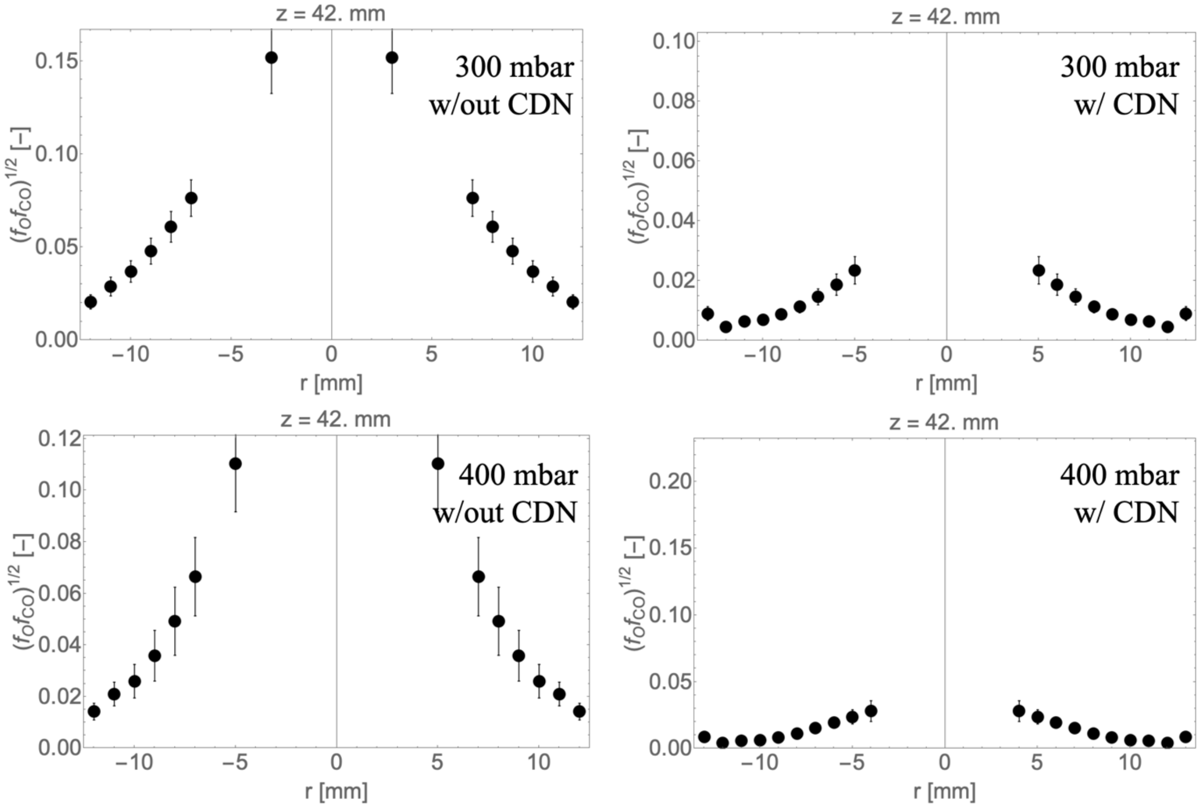

Figure S9 | Product (CO x O) concentration based on emission profile 42 mm downstream from plasma as measured by flame band spectroscopy without and with CDN for ϕ = 5 slm at two pressures, p = 300 and 400 mbar as a function of the radial position in the quartz tube.

Figure S9 shows $(f_O f_{CO})^{1/2}$, representing the product of the molar fraction of O and CO shown as a function of the radial position in the quartz tube.

S.3.3 Infrared Thermography

ImageIR, an infrared (IR)-thermographic camera equipped with a 50 mm lens, uses an open calibrated filter position with a spectral range of 2 – 5.7 mm to capture all images, which provides the surface temperature of the quartz tube. The emissivity of the quartz tube is determined by comparing the temperature recorded by the IR camera with an identical tube painted with a specialized IR coating with a known high emissivity. This data is then used to calibrate and correct the temperatures. The collected information is used to quantify the power lost to the environment at the height of the plasma and aids in elucidating our understanding of the heat transfer and power loss at the height of the plasma.

S.3.4 Emissivity of the Quartz Tube

To correct the temperature (T) of the quartz tube to ensure that the measured temperature is accurate, a calibration for the emissivity was performed using IRBIS. The emissivity of the quartz tube was determined by comparing the temperature recorded by the IR camera with an identical tube painted with a specialized *Lab IR Paint* coating with a known high emissivity.

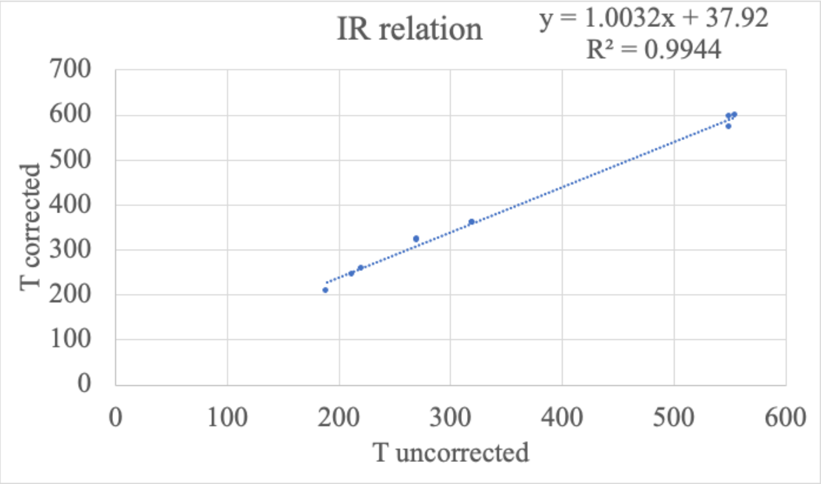

Figure S10 | IR calibration for quartz tube temperature to correct emissivity, allowing for accurate measurement of the temperature used to calculate the power loss to the environment.

Figure S10 shows a good correlation between the corrected temperatures against the measured temperatures. This data was then used to calibrate and correct the recorded temperatures used in calculating the power loss to the environment.

S.3.5 Power Loss to Environment

The power lost to the environment is calculated using the *Stefan-Boltzmann Law*, which gives the total energy radiating from the surface of a blackbody, relating the radiation to the thermodynamic temperature, T.

The radiative power lost (P_{rad}, W) is added to the power lost due to advective heat transfer to the environment (P_{adv}, W):

$$P = P_{rad} + P_{adv} = A\varepsilon\sigma(T^4 - T_{env}^4) + \omega A(T - T_{env}) \tag{S.E7}$$

where A is the surface area (m^2), ε is the emissivity calculated from the calibration of the quartz tube, ΔT is the difference between the corrected temperature of the surface of the quartz tube and environmental temperature (T_{env}, 300 K), and σ is the Stefan-Boltzmann constant (5.67 x 10^{-8} W.m^{-2}K^{-4}). The heat transfer coefficient of the gas to quartz tube, ω, was assumed to be 10 W(m^{2}K)$^{-1}$ but could be between 5 – 37 W(m^{2}K)$^{-1}$ [10]. Using these extreme values, a maximum deviation of ~75 W of power loss is found, which is only 5% of the total input power. *Figure S11* shows the results for the two flow rates, ϕ = 5 and 15 slm, as a function of pressure (mbar).

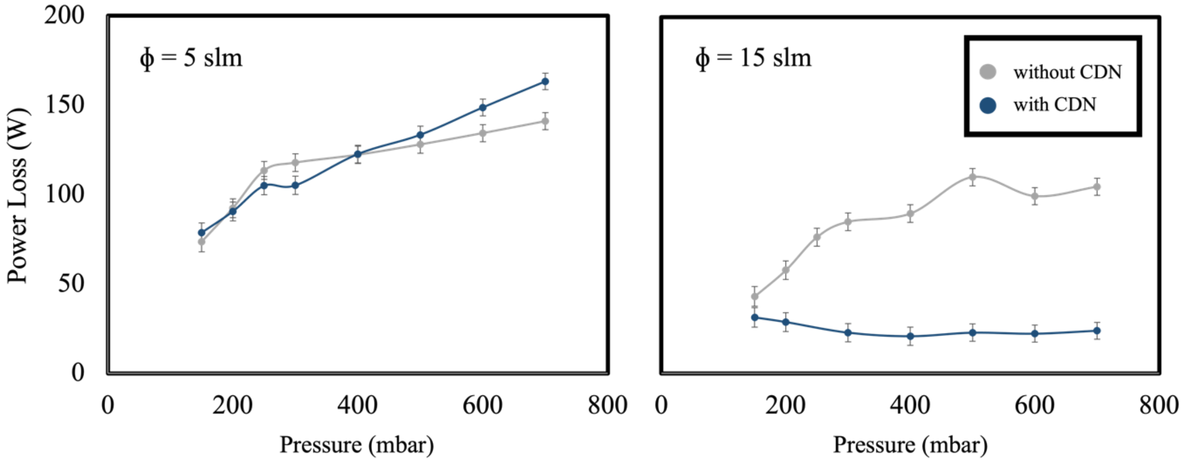

Figure S11 | A comparative look at the calculated power loss within the waveguide (P), calculated from IR thermography measurements, as a function of pressure with and without the CDN. The overall power lost at the height of the plasma drops considerably with the introduction of the CDN at higher flow rates but remains roughly the same for lower flow rates.

Figure S11 shows the calculated power (P) loss as a function of pressure measured by IR thermography for two different flow rates without and with the CDN. Notably, at a ϕ = 15 slm, there is a significant decrease in the power loss to the environment when the CDN is used compared to without the CDN. Conditions without a CDN have a considerably more significant heat loss to the environment at the height of the plasma, resulting in less α. Although the CDN seems to extend the cooling trajectory post-CDN at ϕ = 15 slm, while still leading to higher α, lending to the assumption that the power not being lost to the environment is contributing to thermal α, therefore producing more CO pre-CDN. However, the power loss to the environment is still only 80 W at 700 mbar, representing ~6% of the total input power. Even if this additional power is directly converted to CO, it could not account for the observed ~20% increase in α. Consequently, we can conclude that the power loss does not have a significant effect on the production of CO. These results serve to confirm the presence of a cool sheath of gas from the vortex at higher flow rates when the CDN is present, which explains the reduction in energy lost to the environment. It is also evident that this is only mildly pressure-sensitive at higher flow rates. A reduction in heat loss to the environment results in a drop in the average temperature at the height of the plasma, which partially explains the higher (thermal) α when the CDN is introduced.

S.3.6 Thermocouple Measurements

K-type thermocouples were used to measure the gas temperature within the Faraday cage, at the gas inlet in the primary manifold, and below the mixing nozzle at 220 mm and 450 mm from the plasma. The temperature range of the thermocouples is 75 – 1600 K.

Although the measured temperature of the thermocouples is not equal to the gas temperature due to convective and radiative heat transfer with the gas, the effect for temperatures below 1000 K is expected to be low [11]. Due to the expected turbulent mixing of the gas, the recorded temperatures are considered the average temperature of the mixture downstream of the plasma, with an error of ± 50 K.

Section S.4 Analytical Techniques

S.4.1 Gas Chromatography

Gas Chromatography (GC) is the primary analytical technique for determining the effluent mixture. The measured composition allows for calculating the conversion (α). An InterScience Compact GC 4 was utilized to measure the gas composition by separating a fraction of the effluent, which is then passed through four specialized columns (Molsieve 5A (10 m*0.53 mm), Rt-Q-Bond (4 m*0.32 mm ID), CP-PoraBOND Q (20 m*0.32 mm ID), and Rt-Q-Bond (2m*0.32 mm)).

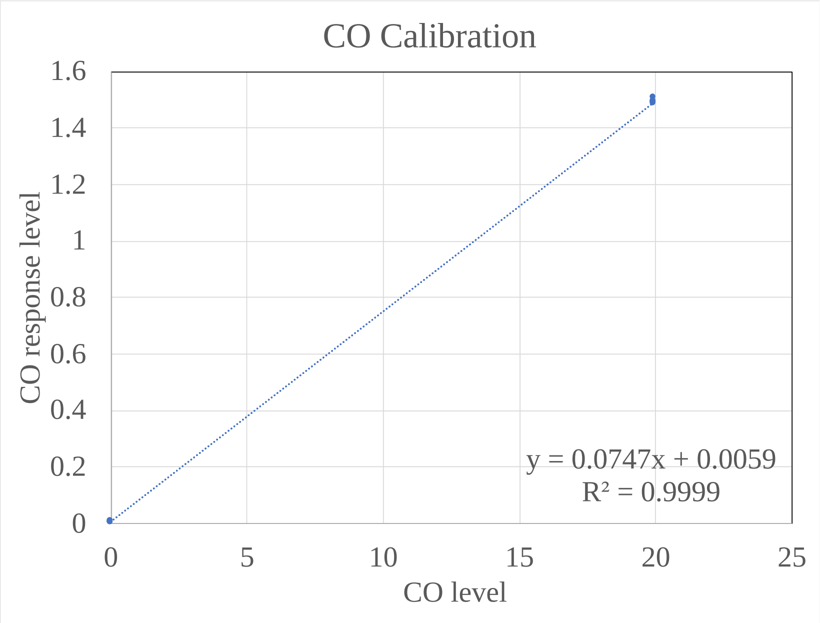

Figure S12 | Calibration for CO as measured by GC.

Figure S12 shows the linear calibration for CO based on the response recorded on GC. Two samples were taken for each measurement, and the GC standard error was calculated for the complete data set.

S.4.2 O_2 Sensor

A secondary measurement of the partial pressure of O_2 in the effluent gas was measured using a Pyroscience FDO2 Optical Oxygen Sensor. The FDO2 sensor utilizes a robust technique called luminescent quenching. A sensor dye is excited with red light and is measured. The presence of O_2 quenches the luminescence, causing a change in the intensity. This is measured and converted to the partial pressure of O_2. Measurements are ~ 3 m downstream of the plasma; thus, the effluent mixture is locked. It is not cross-sensitive to any of the gases used during these experiments and, therefore, can be trusted as a secondary measurement source to ensure accurate values for conversion. The measurement time is under 2.0 s and has an accuracy of ±0.5% O_2 under the conditions outlined in this work.

The coupling of gas chromatography with an oxygen sensor allows for reliable and accurate reading of the post-plasma gas composition.

Section S.5 Key Performance Indicators: Degree of Dissociation and Efficiency of Process

The conversion (α) of CO_2 to CO is described using the net stoichiometric ratios of the reduction reaction:

$$CO_2 \rightarrow (1-\alpha)CO_2 + \alpha CO + \frac{\alpha}{2}O_2 \,, \qquad \text{[S.R1]}$$

of which the values are accurately measured from the effluent using gas chromatography.

The specific energy input (SEI) (eV.molecule^{-1}) is defined by the input power to the system (kJ.s^{-1}) divided by the particle flux of the total inlet flow rate of CO_2:

$$SEI = \frac{P}{N_{mol}.N_A(molecule.mol^{-1})} \times 6.24 \times 10^{21}(eV.kJ^{-1}) \times 60\ (s.min^{-1}) \qquad \text{[S.E8]}$$

Since the molar volume of a gas depends of the temperature and pressure, N_{mol} must be defined as the molar volume (V_{molar}) of an ideal gas under standard conditions (STP, 22.709, L.mol^{-1}), and is calculated by dividing the flow rate in Standard Liters per Minute (ϕ_{slm}) by V_{molar}:

$$N_{mol} = \frac{\phi_{slm}}{V_{molar}} \qquad \text{[S.E9]}$$

The conversion, or dissociation degree, defined as alpha (α), is considered by the mole fraction of target species, CO:

$$\alpha = \frac{\chi_{CO}}{\chi_{CO}+\chi_{CO_2}} \quad \text{[S.E10]}$$

The conversion is calculated based on the mole fraction of CO (equation S.E11), where the mole fraction (χ_i) of a species (i) in the effluent is calculated as:

$$\chi_i = \frac{n_i}{\sum_i n_i}. \quad \text{[S.E11]}$$

In general, the net reaction required to produce a single CO molecule in the dissociation of CO_2 is represented as:

$$CO_2 \rightarrow CO + \frac{1}{2}O_2, \Delta H = 2.93\ eV. \quad \text{(S.R2)}$$

Thus, the energy efficiency (η) of conversion is calculated by coupling the conversion (α), to the formation enthalpy of the net reaction (S.R2) over the SEI, which is a measure of how well the given conditions perform:

$$\eta = \alpha \frac{\Delta H_f}{SEI}. \quad \text{[S.E12]}$$

Section S.6 Modeling Details

To calculate the gas flow velocity, we apply the Menter's Shear Stress Transport (SST) model [12], which uses the standard k-ε model in the free stream and combines it with the more accurate k-ω model near the walls, where the flow is more complicated.

This approach includes the following equations for the turbulent kinetic energy k and the specific dissipation ω:

$$\rho\left(\overrightarrow{u_g}.\nabla\right)k = \nabla\cdot[(\mu+\mu_T\sigma_k)\nabla k]+P-\beta_0\rho\omega k \qquad \text{[S.E13]}$$

$$\rho\left(\overrightarrow{u_g}.\nabla\right)\omega = \nabla\cdot[(\mu+\mu_T\sigma_\omega)\nabla\omega]+\frac{\gamma}{\mu_T}\rho P-\beta_0\rho\omega^2+2(1-f_{v1})\frac{\sigma_{\omega 2}\rho}{\omega}\nabla k\cdot\nabla\omega \qquad \text{[S.E14]}$$

Where ρ stands for the gas density, $\overrightarrow{u_g}$ is the gas flow velocity vector, μ is the dynamic viscosity, σ_k, σ_ω and γ are model coefficients defined in equations S.E22, S.E23, and S.E24 below, and β_0 and $\sigma_{\omega 2}$ are dimensionless model constants defined in Table S.T2. The other symbols are explained below. In equations S.E13 and S.E14, μ_T is the turbulent viscosity of the fluid and is defined as:

$$\mu_T = \frac{a_1 k}{max(a_1\omega, S f_{v2})} \qquad \text{[S.E15]}$$

In which S is the absolute strain rate and a_1 is a dimensionless model constant, defined in table S.T2. In equations S.E13 and S.E14, f_{v1} and f_{v2} are two blending functions that control the switch from the k-ω model to the k-ε model in the free stream (where f_{v1} = 1)

$$f_{v1} = \tanh\left(\min\left(\theta_2^2, \frac{4\sigma_{\omega2}k}{CD_{k\omega}y^2}\right)\right)^4 \qquad [\text{S.E16}]$$

$$f_{v2} = \tanh(\theta_2^2) \qquad [\text{S.E17}]$$

In which y is the y-component of the position vector, and θ_2 and $CD_{k\omega}$ are placeholders for the following terms:

$$CD_{k\omega} = max\left(2\rho\sigma_{\omega2}\frac{1}{\omega}\frac{\partial k}{\partial x}\frac{\partial\omega}{\partial x},\ 10^{-10}\right) \qquad [\text{S.E18}]$$

$$\theta_2 = max\left(\frac{2\sqrt{k}}{\beta_0\omega l_W^2}, \frac{500\mu}{y^2\omega}\right), \qquad [\text{S.E19}]$$

in which l_W is the wall distance. In equations S.E13 and S.E14, P serves as a product limiter coefficient and is defined as:

$$P = \min(P_k 10\rho\beta_0 k\omega), \qquad [\text{S.E20}]$$

in which P_k is a placeholder for the following term:

$$P_k = \mu_T\left(\nabla\overrightarrow{u_g}: \left(\nabla\overrightarrow{u_g} + \left(\nabla\overrightarrow{u_g}\right)^T\right) - \frac{2}{3}\cdot\left(\nabla\cdot\overrightarrow{u_g}\right)^2\right) - \frac{2}{3}\rho k\nabla\cdot\overrightarrow{u_g}. \qquad [\text{S.E21}]$$

The model coefficients in equations S.E13 and S.E14 are defined as:

$$\sigma_k = f_{v1}\cdot\sigma_{k1} + (1 - f_{v1})\sigma_{k2}, \qquad [\text{S.E22}]$$

$$\sigma_\omega = f_{v1} \cdot \sigma_{\omega 1} + (1 - f_{v1})\sigma_{\omega 2}, \qquad \text{[S.E23]}$$

$$\gamma = f_{v1} \cdot \gamma_1 + (1 - f_{v1})\gamma_2, \qquad \text{[S.E24]}$$

in which σ_{k1}, σ_{k2}, $\sigma_{\omega 1}$,$\sigma_{\omega 2}$, γ_1 and γ_2 are dimensionless model constants, defined in table S.T2.

Table S.T2: Dimensionless model constants used in the SST turbulent flow model.

σ_{k1}	0.85
σ_{k2}	1
$\sigma_{\omega 1}$	0.5
$\sigma_{\omega 2}$	0.856
γ_1	0.5556
γ_2	0.44
a_1	0.31
β_0	0.09

References

[1] G. P. Smith *et al.*, “Gri-Mech 3.0.” http://www.me.berkeley.edu/gri_mech/.

[2] S. McBride, B.J., Zehe, M.J., and Gordan, “NASA Glenn Coefficients for Calculating Thermodynamic Properties of Individual Species,” 2002.

[3] V. A. Legasov *et al.*, “A nonequilibrium plasma-chemical process of CO2 dissociation in high-frequency and ultrahigh-frequency discharges,” *Sov. Phys. Dokl.*, vol. 23, p. 44, Jan. 1978.

[4] T. W. H. Righart, “Gas Temperatures adn Residence Times in a Vortex Stabilized CO2 Microwave Plasma,” TU/e, 2018.

[5] A. J. Wolf, T. W. H. Righart, F. J. J. Peeters, P. W. C. Groen, M. C. M. Van De Sanden, and W. A. Bongers, “Characterization of CO2 microwave plasma based on the phenomenon of skin-depth-limited contraction,” *Plasma Sources Sci. Technol.*, vol. 28, no. 11, 2019, doi: 10.1088/1361-6595/ab4e61.

[6] G. J. C. Raposo *et al.*, “Flame Bands: CO + O chemiluminescence as a measure of gas temperature,” *J. Phys. D. Appl. Phys.*, 2021, [Online]. Available: http://iopscience.iop.org/article/10.1088/1361-6463/ac0924.

[7] M. Slack and A. Grillo, “High temperature rate coefficient measurements of CO + O chemiluminescence,” *Combust. Flame*, vol. 59, no. 2, pp. 189–196, 1985, doi: https://doi.org/10.1016/0010-2180(85)90024-0.

[8] W. J. Hooker and R. C. Millikan, “Shock-Tube Study of Vibrational Relaxation in Carbon Monoxide for the Fundamental and First Overtone,” *J. Chem. Phys.*, vol. 38, no. 1, pp. 214–220, 1963, doi: 10.1063/1.1733464.

[9] A. J. Wolf, “Thermal aspects of CO2 conversion in the vortex-stabilized microwave plasma.,” Technische Universiteit Eindhoven, 2020.

[10] V. A. Kurganov, “HEAT TRANSFER COEFFICIENT,” *Themopedia*, 2011. .

[11] B. Liu, Q. Huang, and P. Wang, “Influence of surrounding gas temperature on thermocouple measurement,” *Case Stud. Therm. Eng.*, vol. 19, p. 100627, 2020, doi: https://doi.org/10.1016/j.csite.2020.100627.

[12] F. R. Menter, M. Kuntz, and R. Langtry, “Ten Years of Industrial Experience with the SST Turbulence Model Turbulence heat and mass transfer,” *Cfd.Spbstu.Ru*, vol. 4, no. July 2014, pp. 625–632, 2003.